ACS Photonics

Article

pubs.acs.org/journal/apchd5

Nitrogen-Doped Graphene/Platinum Counter Electrodes for Dye-Sensitized Solar Cells

Chin-An Lin,[†,‡] Chuan-Pei Lee,[‡] Shu-Te Ho,[†] Tzu-Chiao Wei,[‡] Yu-Wen Chi,[§] K. P. Huang,[§] and Jr-Hau He*[,†]

[†]Computer, Electrical and Mathematical Sciences and Engineering (CEMSE) Division, King Abdullah University of Science & Technology (KAUST), Thuwal 23955-6900, Saudi Arabia

[‡]Institute of Photonics and Optoelectronics, and Department of Electrical Engineering, National Taiwan University, Taipei, Taiwan, ROC

[§]Mechanical and Systems Research Laboratories, Industrial Technology Research Institute, Hsinchu, Taiwan, ROC

S *Supporting Information*

ABSTRACT: Nitrogen-doped graphene (NGR) was utilized in dye-sensitized solar cells for energy harvesting. NGR on a Pt-sputtered fluorine-doped tin oxide substrate (NGR/Pt/FTO) as counter electrodes (CEs) achieves the high efficiency of 9.38% via the nitrogen doping into graphene. This is due to (i) the hole-cascading transport at the interface of electrolyte/CEs via controlling the valence band maximum of NGR located between the redox potential of the I^-/I^- redox couple and the Fermi level of Pt by nitrogen doping, (ii) the extended electron transfer surface effect provided by large-surface-area NGR, (iii) the high charge transfer efficiency due to superior catalytic characteristics of NGR via nitrogen doping, and (iv) the superior light-reflection effect of NGR/Pt/FTO CEs, facilitating the electron transfer from CEs to I_3^- ions of the electrolyte and light absorption of dye. The result demonstrated that the NGR/Pt hybrid structure is promising in the catalysis field.

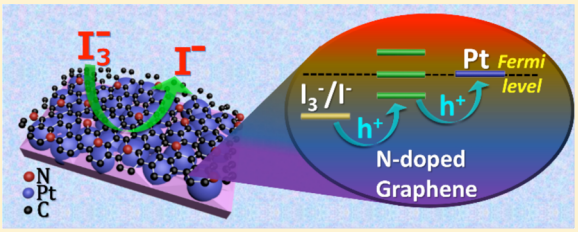

KEYWORDS: *counter electrode, dye-sensitized solar cells, nitrogen-doped graphene, platinum*

Dye-sensitized solar cells (DSSCs) demonstrate a variety of advantages as compared with other types of photovoltaic devices, such as simple fabrication processes in ambient conditions, semitransparency and colorfulness, possible plasticity, and high conversion efficiencies especially under indoor illumination.[1,2] A typical DSSC consists of a dye-sensitized mesoporous titania (TiO_2) photoanode, an electrolyte containing a triiodide/iodide (I_3^-/I^-) redox couple, and a counter electrode (CE) using sputtered platinum (Pt).

The CE, a crucial part of DSSCs, should possess (i) a minimum resistance for collecting electrons from an external circuit to the redox electrolyte, (ii) an excellent catalytic ability for the reduction of triiodide to iodide ions, and (iii) high exchange current densities for effective reduction of the oxidized species, which make the cell a complete circuit. Pt is the most conventional catalytic material for the CEs of DSSCs attributed to its inherent properties of high electron conductivity,[2] catalytic activity,[1] and chemical stability.[2] Thus, developing Pt-composited CEs without sacrificing original catalytic activity and electron conductivity of Pt is a promising way to boost the efficiency of DSSCs.

Two-dimensional (2D) nanomaterials (e.g., graphene (GR) and molybdenum sulfide) enlighten a promising future in next-generation electronics and photonics,[3−7] benefiting from their unique planar advantages, such as the existence of quantum confinements and the absence of interlayer interactions,[8] and thus allow us to achieve smaller, more flexible, and more efficient nanodevices.[9] GR added to a single layer of graphite and made up of sp^2-hybridized carbon atoms arranged into a honeycomb lattice has attracted great attention due to its rich physical phenomena and unique 2D geometric structures and has been well confirmed as a good catalyst for CEs in DSSCs due to its high electrocatalytic area.[9,10] Recently, theoretical studies have revealed that the electronic property and chemical reactivity of nitrogen-doped graphene (NGR) are capable of being tailored, because of the stronger electronegativity of a nitrogen atom than that of a carbon one and increased conjugation between lone-paired electrons of nitrogen atoms and the π-system of GR.[11−13] Therefore, NGR is expected to show more advantages for the catalysis field as compared with pristine GR.

NGR foam-coated conductive glasses have been employed as a CE for DSSCs with the I_3^-/I^- redox couple and N719 dye sensitizer, demonstrating a promising power conversion efficiency (η) of 7.07%.[14] However, the η of DSSCs with NGR foams is limited by a poor fill factor (FF = 0.58). Meanwhile, Ju et al. reported that a DSSC together with a

Received: June 19, 2014
Published: November 10, 2014

   dx.doi.org/10.1021/ph500219r | *ACS Photonics* 2014, 1, 1264−1269

nanoplatelet-NGR CE, a redox couple of $Co(bpy)_3^{3+/2+}$, and an organic sensitizer (O-alkylated-JK-225-organic dye) exhibits a FF of 0.74 and a η of 9.05%, whereas the DSSC with Pt CEs shows values of only 0.71 and 8.43% for FF and η, respectively.[15] Although GR and NGR have been studied for the utilization of CEs in DSSCs, the pertinent η values of the DSSCs with the I_3^-/I^- redox couple and N719 dye sensitizer are still low (4.99 and 7.07% by GR and NGR CEs, respectively), as compared to conventional Pt.[10,14] This is because GR has poorer conductivity and much weaker catalytic activity than Pt. Accordingly, Guai et al. have developed a GR/Pt cocatalysis system for the CEs of DSSCs to enhance the electrocatalytic area by introducing GR into Pt-sputtered fluorine-doped tin oxide (SnO_2:F, FTO) substrates.[16] As compared to conventional Pt/FTO CEs, the GR/Pt/FTO not only reduces the usage amount of Pt by 66% but also exhibits a comparable photovoltaic performance.[16] Furthermore, it is reported that after nitrogen doping in GR, the Fermi level (E_F) shifts above the Dirac point[17,18] and the density of state near the E_F is suppressed.[12,19] Thus, the band gap between the conduction band and the valence band will be opened.[20,21] Moreover, it is found that the split valence band maximum (VBM) of NGR is located between the redox potential of the I_3^-/I^- redox couple and the E_F of Pt, which expectedly could facilitate the hole-cascading transport from the redox couple to NGR/Pt/FTO CEs, reduce the energy loss occurring at the interface of the electrolyte/CEs, and thus increase the performance of DSSCs.[20,22] In addition, it has been evaluated that NGR supports can increase the durability and activity of a Pt catalyst based on density functional theory.[23]

In this work, we prepared an NGR/Pt/FTO CE for (i) suppressing energy loss at the interface of the electrolyte/CE via forming hole cascading structures, (ii) superior electrocatalytic characteristics via nitrogen doping into GR, (iii) providing extended electron transfer surface (EETS) for reduction reactions due to the high surface areas of NGR nanosheets, and (iv) increasing the light-harvesting characteristics of pertinent DSSCs via superior light-reflection abilities. The DSSC with NGR/Pt/FTO CEs exhibits an η of 9.38%, superior to the DSSCs with Pt/FTO CEs (7.53%) and NGR/FTO CEs (5.84%). This result broadens the application of NGR/Pt hybrid structures in the catalysis field.

RESULTS AND DISCUSSION

The X-ray photoelectron spectrum (XPS) characterization of the as-synthesized NGR is performed to analyze the elemental composition and binding configuration of NGR (Figure 1a and b). The atomic percentage of nitrogen in NGR is close to 5.20% with respect to carbon. The asymmetric high-resolution spectrum of nitrogen 1s is deconvoluted into four peaks, as shown in Figure 1a. While a nitrogen atom is doped into GR, it has three common bonding configurations within the carbon lattice, including graphitic (or quaternary), pyridinic, and pyrrolic nitrogen atoms, as shown in Figure 1c. Specifically, a pyridinic nitrogen atom bonded with two carbon atoms at edges or defects of GR would contribute one p electron to the π system. Each pyrrolic nitrogen (cf. a single nitrogen atom) contributes two p electrons to the π system in spite of unnecessary bonds into the five-membered ring, as in pyrrole.[21] Each quaternary nitrogen substitutes for one carbon atom in the six-membered ring. Among these types of nitrogen coordinations, both pyridinic nitrogen and quaternary nitrogen are sp^2 hybridized, and the pyrrolic nitrogen is sp^3 hybridized.

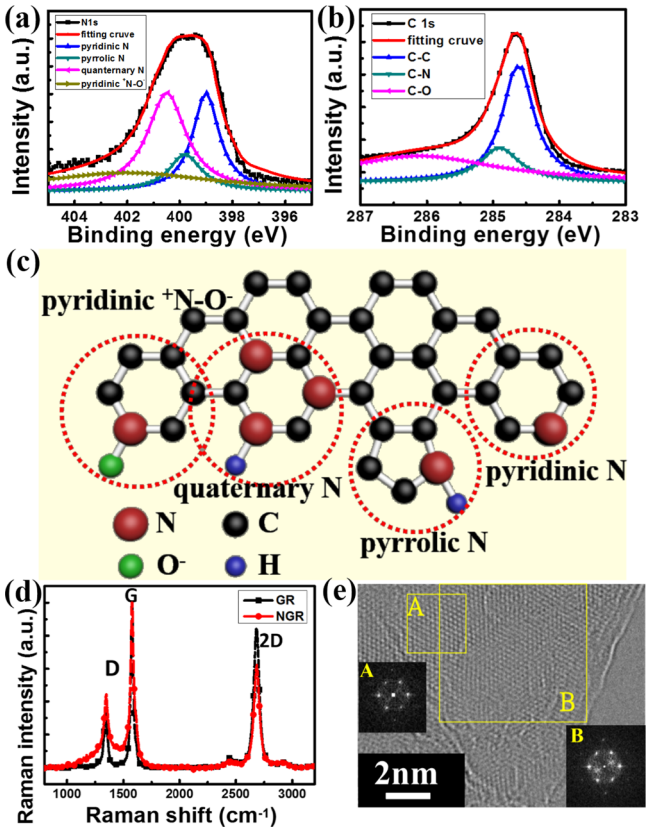

Figure 1. High-resolution XPS spectra: (a) N 1s and (b) C 1s of NGR. (c) Bonding configurations for nitrogen atoms in NGR. (d) Raman spectra of GR and NGR. (e) HRTEM images of NGR. The insets (A and B) in (e) are the SAED patterns of NGR from the different regions.

Pyridinic nitrogen, pyrrolic nitrogen, and graphitic nitrogen have been demonstrated to be significant contributors to the electrocatalytic activity of NGR.[24−26] In Figure 1b, the asymmetric high-resolution spectrum of C 1s is deconvoluted into three peaks, which can be assigned respectively to the C−C (284.6 eV), C−N (285.2 eV), and C−O (286 eV) bonds.[27] One can see that C−C (284.6 eV) representing graphitic carbon dominates in NGR.

Figure 1d shows the Raman spectra for the GR before and after doping with nitrogen. GR exhibits a prominent G band at 1575.9 cm^{-1} assigned to the first-order scattering of the E_{2g} mode observed for sp^2 carbon domains and a broad D band at 1342.9 cm^{-1} caused by sp^3-hybridized carbon (such as structural defects, amorphous carbon, and edge planes) that can reduce the symmetry and break the selection rule.[28] In Figure 1d, the relatively increased intensity of the D band for NGR without shifting its position indicates that the content of disordered carbon increases after plasma treatment, mainly caused by nitrogen doping.[27] A 2D band centered at 2682.5 cm^{-1} is associated with two-phonon intervalley double resonance scattering involving an iTO phonon near the K point.[29,30] Meanwhile, the NGR shows a higher intensity ratio of the D band to the G band (I_D/I_G = 0.85) than pristine GR (I_D/I_G = 0.43), which indicates that the NGR possesses a higher defect density than GR.[30] It is known that a high defect density in carbon materials would be beneficial for their electrocatalytic activity.[31] The photovoltaic characteristics of DSSCs with CEs using GR and NGR are compared as shown in

dx.doi.org/10.1021/ph500219r | ACS Photonics 2014, 1, 1264−1269

Figure S1, and their corresponding photovoltaic parameters are listed in Table S1. Obviously, the DSSC with an NGR CE exhibits a higher η of 5.84% than the DSSC with a GR CE (2.94%). Figure 1e shows the high-resolution transmission electron microscopy (HRTEM) images of NGR indicating a typical wrinkled structure. The insets (A and B) are the selected area electron diffraction (SAED) patterns of NGR.[32] The well-defined diffraction spots in the SAED patterns have confirmed the crystalline structure of the NGR.

The surface morphology of Pt/FTO and NGR/Pt/FTO CEs is characterized using scanning electron microscopy (SEM). The SEM image in Figure 2a shows the Pt nanoparticles

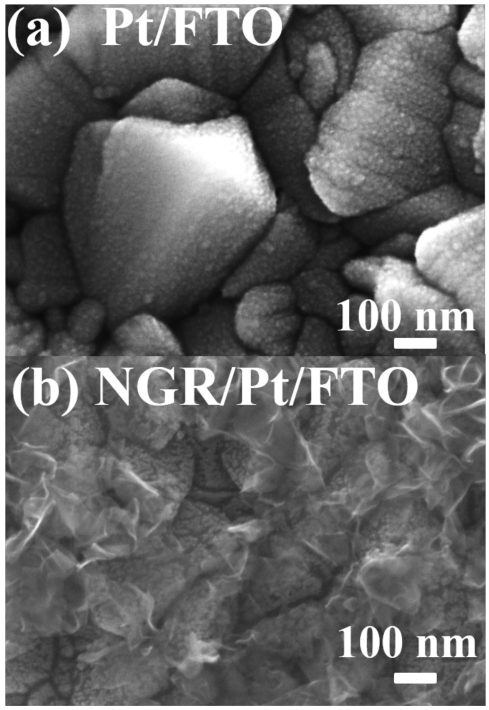

Figure 2. SEM images of (a) Pt/FTO and (b) NGR/Pt/FTO CEs.

uniformly distributed on the FTO substrate. One should note that the effective catalytic area of the Pt/FTO CE would be mainly determined by the roughness of FTO. Figure 2b shows the SEM image of an NGR/Pt/FTO CE. The surface morphologies of both the Pt nanoparticles and the NGR layers can be clearly observed in Figure 2b, which indicates that the NGR/Pt/FTO CE not only keeps the original catalytic area of Pt/FTO but also additionally possesses an EETS due to the high surface area provided by NGR nanosheets. Lee et al. have demonstrated that titanium carbide (TiC) was added to an ionic liquid-based electrolyte to form an EETS from the CE's surface to the bulk electrolyte.[33] It was found that the resistance of the charge-transfer process at the Pt CE (R_{CT}) decreased when TiC was added, which was confirmed by electrochemical impedance spectroscopy (EIS) analysis. EETS facilitates electron transfer from the CE to I_3^- ions of the electrolyte and thereby enables the redox couple to work more efficiently.[33−35]

UV−visible spectroscopy is used to study the light reflection behaviors for Pt/FTO and NGR/Pt/FTO CEs. The total reflectance (R), total transmittance (T), and absorptance (A) spectra of dye/TiO_2/FTO, Pt/FTO, and NGR/Pt/FTO electrodes are shown in Figure S2. The absorptance is extracted from the following formula: A (%) = 100 (%) − Total R (%) − Total T (%). After calculation, the enhancement of the total reflectance spectrum is presented in Figure S3. As shown in Figure S2, the total reflectance is enhanced from 11.94% to 13.92% at 540 nm after depositing the NGR on the Pt nanoparticles. The total T spectrum of dye/TiO_2/FTO electrodes as shown in Figure S2(a) indicates that the dye/TiO_2/FTO electrodes still have ca. 7% and 10−17% light loss in the wavelength range 400−650 nm and 650−800 nm, respectively. Therefore, the light reflectance ability of CEs is an important part for DSSCs in harvesting nonabsorbed light. On the other hand, Figure S2(b) also shows the UV−visible spectra of NGR/Pt/FTO and Pt/FTO CEs. Obviously, the A of NGR/Pt/FTO CEs is lower than that of Pt/FTO CEs below 650 nm. The NGR/Pt/FTO CE possesses superior light reflection ability to that of the Pt/FTO CE, which benefits harvesting of nonabsorbed light and enhances the photocurrent of the pertinent cells. Moreover, the enhancement of the total R spectrum is shown in Figure S3, which is extracted from the following formula: (total $R_{NGR/Pt/FTO}$ − total $R_{Pt/FTO}$) × 100%/$R_{Pt/FTO}$. Note that the enhancement of total R is ca. 10−25% and 10−50% in the wavelength range 400−650 nm and 650−800 nm, respectively. This result suggests that the NGR/Pt/FTO CE possesses higher light-reflection ability as compared with the Pt/FTO CE. The inset in Figure S3 is the photoimages for Pt/FTO and NGR/Pt/FTO CEs. From these photo images, it can be found that the appearance difference between Pt/FTO and NGR/Pt/FTO due to the reflection difference indicates that the deposition of the NGR layer changes the original optical property of Pt/FTO. The superior light-reflection ability of NGR/Pt/FTO CEs would enhance photon absorption by the dyes and thus enhances the light-harvesting efficiency of the pertinent DSSC.

Photocurrent density−voltage (J−V) characteristics of the DSSCs with Pt/FTO CEs, NGR/Pt/FTO CEs, and NGR CEs are shown in Figure 3a, and the corresponding photovoltaic parameters are summarized in Table 1. The cell with an NGR/

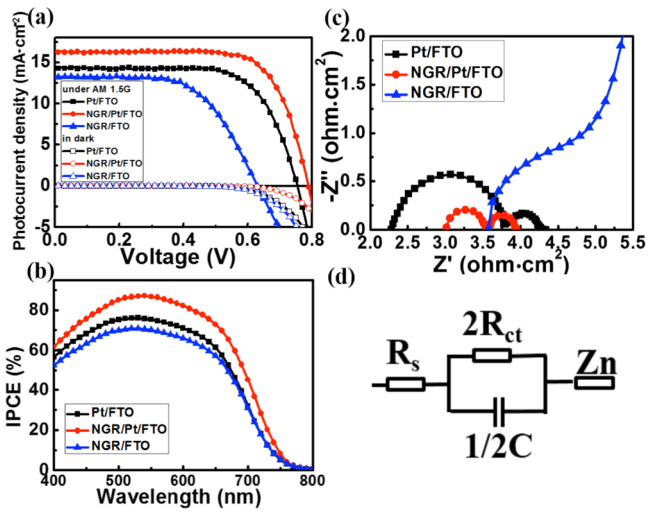

Figure 3. (a) J−V curves of the DSSCs with Pt/FTO, NGR/Pt/FTO, and NGR/FTO CEs, measured both under AM 1.5G illumination (100 mW cm^{-2}) and in the dark. (b) IPCE spectra of the DSSCs with Pt/FTO, NGR/Pt/FTO, and NGR/FTO CEs. (c) Nyquist plots obtained from EIS measurement for symmetric cells composed of Pt/FTO, NGR/Pt/FTO, and NGR/FTO electrodes. (d) Equivalent circuit scheme for the analysis of EIS results in (c).

dx.doi.org/10.1021/ph500219r | ACS Photonics 2014, 1, 1264−1269

Table 1. Photovoltaic Parameters of DSSCs with Various CEs Measured under 100 mW cm^{-2} (AM 1.5G) and the Corresponding Values of the Sheet Resistance, R_S, on the Surface of Various Electrodes and of the Charge Transfer Resistance, R_{CT}, at the Electrolyte/CE Interface

CE	R_S (Ω cm^2)	R_{CT} (Ω cm^2)	V_{OC} (mV)	J_{SC} (mA cm^{-2})	FF	η (%)
Pt/FTO	2.30	1.48	755	14.10	0.70	7.53
NGR/Pt/FTO	3.00	0.54	785	16.23	0.74	9.38
NGR/FTO	3.57	2.73	718	13.26	0.61	5.84

Pt/FTO CE shows the best performance, with an η of 9.38%, an open-circuit voltage (V_{OC}) of 785 mV, a fill factor (FF) of 0.74, and a short-circuit current density (J_{SC}) of 16.23 mA cm^{-2}. As compared to the DSSCs with Pt/FTO CEs (7.53%) and NGR CEs (5.84%), the high efficiency of the DSSC with NGR/Pt/FTO CEs is mainly due to its high J_{SC}, FF, and V_{OC}. The related mechanisms for enhanced J_{SC} will be discussed later. A faster movement of the redox couple is expected in the electrolyte of the DSSC with an NGR/Pt/FTO CE due to the faster reduction of I_3^- ions at the CE of the cell, which in turn can lead to faster electron transfer kinetics in the cell and to a higher FF for the cell (0.74), compared to those of the cells with a Pt/FTO CE (0.70) and a NGR CE (0.61). In addition, the faster reduction of I_3^- ions at the CE of the cell would enable reduced availability of I_3^- ions for recombination with injected electrons (see the dark-current density–voltage plots in Figure 3a) and thereby a higher V_{OC} for the cells with an NGR/Pt/FTO CE (785 mV) than those for cells with a Pt/FTO CE (755 mV) and an NGR/FTO CE (718 mV). Furthermore, incident-photon-to-converted-electron (IPCE) curves are measured for the DSSCs with Pt/FTO, NGR/Pt/FTO, and NGR/FTO CEs (Figure 3b). The DSSC with an NGR/Pt/FTO CE exhibits broad IPCE curves covering the visible regions from 400 to 800 nm and the maximum IPCE value of 87% at 540 nm. The maximum IPCE values are 67.7% and 75.7% at 540 nm for the DSSC with NGR/FTO and Pt/FTO CEs, respectively. Note that the introduction of NGR does not influence the shape of the IPCE curves in this study since the same sensitizer (N719) and configuration of the TiO_2 layer were used for the two kinds of DSSCs mentioned above. The trend in IPCE plots is consistent with the corresponding J_{SC} values (Table 1). The enhancement in J_{SC} and IPCE will be discussed below.

Recently, Luo et al. reported that the pyridinic nitrogen efficiently modifies the valence band structure of GR to be upward (more positive).[22] The rising density of p states near the E_F and the reduction of the work function are confirmed by ultraviolet photoemission spectroscopy.[22,36] The band gap of NGR is around 0.38 eV.[20] It should be noted that the redox potential of I_3^-/I^- is lower than the E_F of Pt and the VBM of NGR by 0.45 eV (vs vacuum).[37] According to the literature,[38] the alignment of energy band edges at the interfaces of the redox couple (I_3^-/I^-) and the NGR/Pt/FTO CE is schematically shown in Figure 4a, and the reverse case with Pt/NGR/FTO CE is shown in Figure 4b. A CE with reverse structure, Pt/NGR/FTO, is prepared in comparison with NGR/Pt/FTO CE. Obviously, the case in Figure 4a is thermodynamically appropriate for the operation of the DSSCs as compared with the case in Figure 4b. Figure S4a shows the SEM image of Pt/NGR/FTO. One can clearly see the Pt nanoparticle-coated NGR nanosheets. The J–V characteristics of a DSSC with Pt/

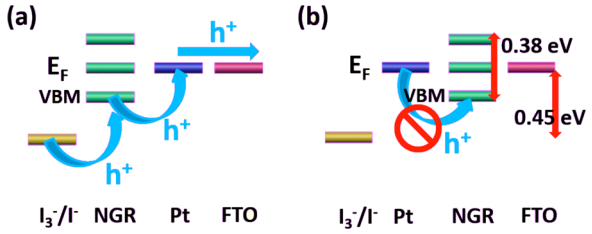

Figure 4. Schematics of the hole transport at the interfaces of (a) I_3^-/I^--based electrolyte/NGR/Pt/FTO and (b) I_3^-/I^--based electrolyte/Pt/NGR/FTO in a DSSC.

NGR/FTO CEs are shown in Figure S4b. The DSSC with a reverse structure, Pt/NGR/FTO, shows an η of 6.81% (with V_{OC} = 745 mV, J_{SC} = 14.92 mA cm^{-2}, and FF = 0.61), which is much lower than the case of NGR/Pt/FTO since NGR/Pt/FTO possesses favorable hole-cascading transport at the electrolyte/CE interface and thus enhances hole injection, leading to a higher J_{SC}. Another possible reason for high J_{SC} is the electron transport between Pt and FTO, which is better than that between FTO and NGR. More details about the band diagram for favorable hole-cascading transport are discussed and shown in Figures S5, S6, and S7 in the Supporting Information. Our previous work also indicates that the introduction of an energy barrier can facilitate the physical hole–electron separation in DSSCs and hybrid solar cells.[39,40] Moreover, the high J_{SC} of the DSSC with an NGR/Pt/FTO CE is partly attributed to the EETS effect and the superior light-reflection effect of the NGR/Pt/FTO CEs as well.

A high-performance CE should have a low resistance and high catalytic activity (i.e., low impedance for charge carrier transfer for the reduction of I_3^- ions at the interface of CEs with the electrolyte). The EIS analysis is utilized to evaluate the impedance of the CEs by using a symmetric cell (CE/electrolyte/CE) with an active area of 1 cm^2. A Randles-type circuit model (Figure 3d) is adopted to estimate the resistance of each interface in the symmetric cell.[41] Figure 3c shows Nyquist plots of the symmetric, sandwich-type cells with Pt/FTO, NGR/Pt/FTO, and NGR/FTO CEs. Via EIS analysis, a symmetric, sandwich-type cell can be divided into three parts. The ohmic series resistance (Rs), i.e., electrical contact and sheet resistance of electrodes, is determined in the high-frequency region (10^6–10^5 Hz) where the phase is zero. The first semicircle in the middle-frequency range (10^5–10 Hz) represents the resistance associated with the heterogeneous charge transfer at the CE/electrolyte interface (R_{CT}). The second semicircle in the low-frequency range (10–0.1 Hz) represents the resistance within the electrolyte (Zn). The values of R_S and R_{CT} are usually adopted to evaluate the resistances of the electrode and the catalytic activity of the electrode for reducing triiodide. The values of R_S and R_{CT} are given in Table 1. The symmetric sandwich-type cells with Pt/FTO, NGR/Pt/FTO, and NGR/FTO show R_{CT} values of 1.48, 0.54, and 2.73 Ω cm^2, respectively, and R_S values of 2.30, 3.00, and 3.57 Ω cm^2, respectively. The results show that EETS provided by an NGR overlayer of NGR/Pt/FTO CE can more effectively catalyze the reduction of I_3^- ions to I^- ions due to its high electrocatalytic ability without greatly scarifying conductivity, leading to the high values of FF and J_{SC} of the cells with NGR/Pt/FTO CEs. Moreover, as the same sensitizer and configuration of the TiO_2 layer were used, the IPCE enhancement without changing the overall curve shape via introducing NGR on Pt/FTO CEs is ascribed to an improved

dx.doi.org/10.1021/ph500219r | ACS Photonics 2014, 1, 1264–1269

hole injection efficiency from the electrolyte into the Pt/FTO and enhanced charge transfer efficiency of CEs.

One should note that although superior performance is certainly achieved, Pt is still needed in this study. More efforts should be put into avoiding using Pt while achieving better CE performance, as one of the main motivations for developing non-Pt CE materials is to lower the cost. For example, earth-abundant electrocatalysts such as CoS_2,[42] Co_9S_8,[43] and MoS_2 have been widely investigated to replace high-cost Pt in DSSCs due to several advantages, such as high catalytic activity, good conductivity, low cost, easy availability, and stability.[44,45] By the combination of earth-abundant electrocatalysts and graphene sheets, high-performance catalytic CEs could be expected for Pt-free DSSCs, which is under investigation.

CONCLUSION

In summary, the DSSC with the NGR/Pt/FTO CE shows a high efficiency of 9.38% via nitrogen doping into graphene. The underlying mechanism is (i) the hole-cascading transport at the interface of electrolyte/CEs, (ii) the EETS provided by the NGR overlayer of NGR/Pt/FTO CEs, (iii) the high charge transfer efficiency due to superior catalytic characteristics of NGR via nitrogen doping, and (iv) the superior light-reflection effect of NGR/Pt/FTO CEs. The results in this work pave a new pathway to explore highly efficient materials for CEs.

METHODS

The synthesis of few-layered GR nanosheets was carried out in a microwave plasma torch deposition system, equipped with a 2 kW and 2.45 GHz microwave source. Argon (2−40 L min^{-1}) was introduced into a quartz tube that is located around the reactive area of the microwave to form a plasma, and a hydrocarbon gas (1−40 sccm of CH_4) was adopted as the precursor to synthesize graphene sheets. As-prepared graphene sheets were treated subsequently with N_2 plasma using a low-pressure plasma-enhanced chemical vapor deposition at room temperature.

GRs and NGRs were dispersed in ethanol to form a concentration of 0.01 g mL^{-1} prior to the use. Glass substrates coated with FTO (SnO_2:F, TEC7, sheet resistance of 8 Ω sq^{-1}) were immersed into a 40 mM $TiCl_4$ (Showa) aqueous solution at 70 °C for 30 min. For the mesoporous double-layer TiO_2 photoanodes, a 12-μm-thick transparent layer (diameter of 20−50 nm, Eversolar P-300) and a 5-μm-thick light-scattering layer (PST-400, JGC Catalysts and Chemicals, Japan) were deposited sequentially by a conventional screen-printing method. The projected area of the TiO_2 film on each photoanode is controlled to be 0.25 cm^2. The TiO_2 photoanodes were heated under air flow at 500 °C for 30 min. Then, the TiO_2 photoanodes were again immersed into a 40 mM $TiCl_4$ aqueous solution at 70 °C for 30 min and sintered at 500 °C for 30 min in ambient conditions. Subsequently, these TiO_2 photoanodes were sensitized in an N719 solution (0.5 mM, Dyesol) for 24 h at room temperature. In this study, four types of counter electrodes, Pt/FTO, GR/FTO, NGR/FTO, and NGR/Pt/FTO CEs, were prepared for comparison of their catalytic performance. For Pt/FTO CE, 8-nm-thick Pt is sputtered on FTO as the control CE. GR and NGR CEs are prepared by the drop-coating method, and 600 μL (10 μL each time) of NGR or GR solutions is used for each coating. The Pt/FTO CE is further coated with NGR nanosheets by using the spin-coating method for preparing an NGR/Pt/FTO CE. After annealing at 200 °C for 20 min, all CEs were assembled with N719 dye-sensitized TiO_2 photoanodes as sandwich-type cells. The two electrodes were separated and sealed with a hot-melt spacer 25 μm in thickness (Dupont). An electrolyte solution consisting of 1.20 M 1,2-dimethyl-3-propylimidazolium iodide (DMPII, Sigma-Aldrich), 0.03 M iodine (I_2, Showa), 0.10 M guanidinium thiocyanate (GuSCN, Sigma-Aldrich), and 0.5 M 4-*tert*-butylpyridine (*t*BP, Sigma-Aldrich) in a mixed solvent of acetonitrile (MP) and valeronitrile (Sigma-Aldrich) (v/v, 85/15) was injected into the assembled cells through the hole on the CEs.[24] The measurements and the instruments are shown in the Supporting Information.

ASSOCIATED CONTENT

Supporting Information

This material is available free of charge via the Internet at http://pubs.acs.org.

AUTHOR INFORMATION

Corresponding Author

*E-mail: jrhau.he@kaust.edu.sa.

Notes

The authors declare no competing financial interest.

REFERENCES

(1) O'Regan, B.; Grätzel, M. A low-cost, high-efficiency solar cell based on dye-sensitized colloidal TiO_2 films. *Nature* **1991**, *353*, 737−740.

(2) Grätzel, M. Photoelectrochemical cells. *Nature* **2001**, *414*, 338−344.

(3) Tsai, D. S.; Liu, K. K.; Lien, D. H.; Tsai, M. L.; Kang, C. F.; Lin, C. A.; Li, L. J.; He, J. H. Few-layer MoS_2 with high broadband photogain and fast optical switching for use in harsh environments. *ACS Nano* **2013**, *7*, 3905−3911.

(4) Yin, Z.; Zhu, J.; He, Q.; Cao, X.; Tan, C.; Chen, H.; Yan, Q.; Zhang, H. Graphene-based materials for solar cell applications. *Adv. Energy Mater.* **2014**, *4*, 1300574−19.

(5) Liu, L.; Tan, C.; Chai, J.; Wu, S.; Radko, A.; Zhang, H.; Mandler, H. Electrochemically "writing" graphene from graphene oxide. *Small* **2013**, DOI: 10.1002/smll.201301953.

(6) Cao, X.; Yin, Z.; Zhang, H. Three-dimensional graphene materials: preparation, structures and application in supercapacitors. *Energy Environ. Sci.* **2014**, DOI: 10.1039/C4EE00050A.

(7) Cao, X.; Zheng, B.; Rui, X.; Shi, W.; Yan, Q.; Zhang, H. Metal oxide-coated three-dimensional graphene prepared by the use of metal−organic frameworks as precursors. *Angew. Chem., Int. Ed.* **2014**, *53*, 1404−1409.

(8) Tsai, D. S.; Lien, D. H.; Tsai, M. L.; Su, S. H.; Chen, K. M.; Ke, J. J.; Yu, Y. C.; Li, L. J.; He, J. H. Trilayered MoS_2 metal−semiconductor−metal photodetectors: photogain and radiation resistance. *IEEE J. Select. Top. Quantum Elect.* **2014**, *20*, 3800206−6.

(9) Yang, P. K.; Chang, W. Y.; Teng, P. Y.; Jen, S. F.; Lin, S. J.; Chiu, P. W.; He, J. H. Fully transparent resistive memory employing graphene electrodes for eliminating undesired surface effects. *Proc. IEEE* **2013**, *101*, 1732−1739.

(10) Roy-Mayhew, J. D.; Bozym, D. J.; Punckt, C.; Aksay, I. A. Functionalized graphene as a catalytic counter electrode in dye-sensitized solar cells. *ACS Nano* **2010**, *4*, 6203−6211.

(11) Cervantes-Sodi, F.; Csanyi, G.; Piscanec, S.; Ferrari, A. C. Edge-functionalized and substitutionally doped graphene nanoribbons: electronic and spin properties. *Phys. Rev.* **2008**, *B77*, 165427−13.

(12) Deifallah, M.; McMillan, P. F.; Cora, F. Electronic and structural properties of two-dimensional carbon nitride graphenes. *J. Phys. Chem. C* **2008**, *112*, 5447−5453.

(13) Li, Y.; Zhou, Z.; Shen, P.; Chen, Z. Spin gapless semiconductor-metal-half-metal properties in nitrogen-doped zigzag graphene nanoribbons. *ACS Nano* **2009**, *3*, 1952−1958.
(14) Xue, Y.; Liu, J.; Chen, H.; Wang, R.; Li, D.; Qu, J.; Dai, L. Nitrogen-doped graphene foams as metal-free counter electrodes in high-performance dye-sensitized solar cells. *Angew. Chem., Int. Ed.* **2012**, *51*, 12124−12127.
(15) Ju, M. J.; Kim, J. C.; Choi, H. J.; Choi, I. T.; Kim, S. G.; Lim, K.; Ko, J.; Lee, J. J.; Jeon, I. Y.; Baek, J. B.; Kim, H. K. N-doped graphene nanoplatelets as superior metal-free counter electrodes for organic dye-sensitized solar cells. *ACS Nano* **2013**, *7*, 5243−5250.
(16) Guai, G. H.; Song, Q. L.; Guo, C. X.; Lu, Z. S.; Chen, T.; Ng, C. M.; Li, C. M. Graphene-counter electrode to significantly reduce Pt loading and enhance charge transfer for high performance dye-sensitized solar cell. *Sol. Energy* **2012**, *86*, 2041−2048.
(17) Lherbier, A.; Blase, X.; Niquet, Y. M.; Triozon, F.; Roche, S. Charge transport in chemically doped 2D graphene. *Phys. Rev. Lett.* **2008**, *101*, 036808−4.
(18) Wu, M.; Cao, C.; Jiang, J. Z. Light non-metallic atom (B, N, O and F)-doped graphene: a first-principles study. *Nanotechnology* **2010**, *21*, 505202−6.
(19) Wei, D.; Liu, Y.; Wang, Y.; Zhang, H.; Huang, L.; Yu, G. Synthesis of N-doped graphene by chemical vapor deposition and its electrical properties. *Nano Lett.* **2009**, *9*, 1752−1758.
(20) Rani, P.; Jindal, V. K. Designing band gap of graphene by B and N dopant atoms. *RSC Adv.* **2013**, *3*, 802−812.
(21) Wang, H.; Maiyalagan, T.; Wang, X. Review on recent progress in nitrogen-doped graphene: synthesis, characterization, and its potential applications. *ACS Catal.* **2012**, *2*, 781−794.
(22) Luo, Z.; Lim, S.; Tian, Z.; Shang, J.; Lai, L.; MacDonald, B.; Fu, C.; Shen, Z.; Yu, T.; Lin, J. Pyridinic N doped graphene: synthesis, electronic structure, and electrocatalytic property. *J. Mater. Chem.* **2011**, *21*, 8038−8044.
(23) Groves, M. N.; Chan, A. S. W.; Malardier-Jugroot, C.; Jugroot, M. Improving platinum catalyst binding energy to graphene through nitrogen doping. *Chem. Phys. Lett.* **2009**, *481*, 214−219.
(24) Matter, P. H.; Zhang, L.; Ozkan, U. S. The role of nanostructure in nitrogen-containing carbon catalysts for the oxygen reduction reaction. *J. Catal.* **2006**, *239*, 83−96.
(25) Maldonado, S.; Stevenson, K. J. Influence of nitrogen doping on oxygen reduction electrocatalysis at carbon nanofiber electrodes. *J. Phys. Chem. B* **2005**, *109*, 4707−4716.
(26) Niwa, H.; Horiba, K.; Harada, Y.; Oshima, M.; Ikeda, T.; Terakura, K.; Ozaki, J. I.; Miyata, S. X-ray absorption analysis of nitrogen contribution to oxygen reduction reaction in carbon alloy cathode catalysts for polymer electrolyte fuel cells. *J. Power Sources* **2009**, *187*, 93−94.
(27) Shao, Y.; Zhang, S.; Engelhard, M. H.; Li, G.; Shao, G.; Wang, Y.; Liu, J.; Aksay, I. A.; Lin, Y. Nitrogen-doped graphene and its electrochemical applications. *J. Mater. Chem.* **2010**, *20*, 7491−7496.
(28) Ferrari, A. C. Raman spectroscopy of graphene and graphite: disorder, electron-phonon coupling, doping and nonadiabatic effects. *Solid State Commun.* **2007**, *143*, 47−57.
(29) Malard, L. M.; Pimenta, M. A.; Dresselhaus, G.; Dresselhaus, M. S. Raman spectroscopy in graphene. *Phys. Rep.* **2009**, *473*, 51−87.
(30) Luo, Z.; Yu, T.; Kim, K. J.; Ni, Z.; You, Y.; Lim, S.; Shen, Z.; Wang, S.; Lin, J. Functionalized graphene as a catalytic counter electrode in dye-sensitized solar cells. *ACS Nano* **2009**, *3*, 1781−1788.
(31) Punckt, C.; Pope, M. A.; Liu, J.; Lin, Y.; Aksay, I. A. Electrochemical performance of graphene as effected by electrode porosity and graphene functionalization. *Electroanalysis* **2010**, *22*, 2834−2841.
(32) Wang, G.; Yang, J.; Park, J.; Gou, X.; Wang, B.; Liu, H.; Yao, J. Facile synthesis and characterization of graphene nanosheets. *J. Phys. Chem. C* **2008**, *112*, 8192−8195.
(33) Lee, C. P.; Lee, K. M.; Chen, P. Y.; Ho, K. C. On the addition of conducting ceramic nanoparticles in solvent-free ionic liquid electrolyte for dye-sensitized solar cells. *Sol. Ener. Mater. Sol. Cells* **2009**, *93*, 1411−1416.
(34) Lee, C. P.; Chen, P. Y.; Vittal, R.; Ho, K. C. Iodine-free high efficient quasi solid-state dye-sensitized solar cell containing ionic liquid and polyaniline-loaded carbon black. *J. Mater. Chem.* **2010**, *20*, 2356−2361.
(35) Lee, C. P.; Lin, L. Y.; Chen, P. Y.; Vittal, R.; Ho, K. C. All-solid-state dye-sensitized solar cells incorporating SWCNTs and crystal growth inhibitor. *J. Mater. Chem.* **2010**, *20*, 3619−3625.
(36) Jun, G. H.; Jin, S. H.; Lee, B.; Kim, B. H.; Chae, W. S.; Hong, S. H.; Jeon, S. Enhanced conduction and charge-selectivity by N-doped graphene flakes in the active layer of bulk-heterojunction organic solar cells. *Energy Environ. Sci.* **2013**, *6*, 3000−3006.
(37) Zhang, S.; Yanagida, M.; Yang, X.; Han, L. Effect of 4-tert-butylpyridine on the quasi-fermi level of dye-sensitized TiO_2 films. *Appl. Phys. Express* **2011**, *4*, 042301−3.
(38) Daeneke, T.; Kwon, T. H.; Holmes, A. B.; Duffy, N. W.; Bach, U.; Spiccia, L. High-efficiency dye-sensitized solar cells with ferrocene-based electrolytes. *Nat. Chem.* **2011**, *3*, 211−215.
(39) Lin, C. A.; Huang, K. P.; Ho, S. T.; Huang, M. W.; He, J. H. An energy-harvesting scheme utilizing Ga-rich $CuIn_{(1-x)}Ga_xSe_2$ quantum dots for dye-sensitized solar cells. *Appl. Phys. Lett.* **2012**, *101*, 123901−4.
(40) Ho, C. R.; Tsai, M. L.; Jhuo, H. J.; Lien, D. H.; Lin, C. A.; Tsai, S. H.; Wei, T. C.; Huang, K. P.; Chen, S. A.; He, J. H. An energy-harvesting scheme employing $CuGaSe_2$ quantum dot-modified ZnO buffer layers for drastic conversion efficiency enhancement in inorganic-organic hybrid solar cells. *Nanoscale* **2013**, *5*, 6350−6355.
(41) Randles, J. E. B. Kinetics of rapid electrode reactions. *Discuss. Faraday Soc.* **1947**, *1*, 11−19.
(42) Faber, M. S.; Dziedzic, R.; Lukowski, M. A.; Kaiser, N. S.; Ding, Q.; Jin, S. High-performance electrocatalysis using metallic cobalt pyrite (CoS_2) micro- and nanostructures. *J. Am. Chem. Soc.* **2014**, *136*, 10053−10061.
(43) Chang, S. H.; Lu, M. D.; Tung, Y. L.; Tuan, H. Y. Gram-scale synthesis of catalytic Co_9S_8 nanocrystal ink as a cathode material for spray-deposited, large-area dye-sensitized solar cells. *ACS Nano* **2013**, *7*, 9443−9451.
(44) Wu, M.; Ma, T. Platinum-free catalysts as counter electrodes in dye-sensitized solar cells. *ChemSusChem* **2012**, *5*, 1343−1357.
(45) Faber, M. S.; Jin, S. Earth-abundant inorganic electrocatalysts and their nanostructures for energy conversion applications. *Energy Environ. Sci.* **2014**, DOI: 10.1039/C4EE01760A.